Cécile Patte
Inria,
Palaiseau 91120, France;
Laboratoire de Mécanique des Solides,
École Polytechnique/CNRS/IPP,
Palaiseau 91120, France
e-mail: cecile.patte@inria.fr

Pierre-Yves Brillet
Hypoxie et Poumon,
Université Sorbonne Paris Nord/INSERM,
Bobigny 93022, France;
Hôpital Avicenne,
APHP,
Bobigny 93022, France
e-mail: pierre-yves.brillet@aphp.fr

Catalin Fetita
SAMOVAR,
Telecom SudParis/Institut Mines-Télécom/IPP,
Évry 91042, France
e-mail: catalin.fetita@telecom-sudparis.eu

Jean-François Bernaudin
Hypoxie et Poumon,
Université Sorbonne Paris Nord/INSERM,
Bobigny 93022, France
e-mail: jean-francois.bernaudin@sorbonne-universite.fr

Thomas Gille
Hypoxie et Poumon,
Université Sorbonne Paris Nord/INSERM,
Bobigny 93022, France;
Hôpital Avicenne,
APHP,
Bobigny 93022, France
e-mail: thomas.gille@aphp.fr

Hilario Nunes
Hypoxie et Poumon,
Université Sorbonne Paris Nord/INSERM,
Bobigny 93022, France;
Hôpital Avicenne,
APHP,
Bobigny 93022, France
e-mail: hilario.nunes@aphp.fr

Dominique Chapelle
Inria,
Palaiseau 91120, France;
Laboratoire de Mécanique des Solides,
École Polytechnique/CNRS/IPP,
Palaiseau 91120, France
e-mail: dominique.chapelle@inria.fr

Martin Genet
Laboratoire de Mecanique des Solides,
École Polytechnique/CNRS/IPP,
Palaiseau 91120, France;
Inria,
Palaiseau 91120, France
e-mail: martin.genet@polytechnique.edu

Estimation of Regional Pulmonary Compliance in Idiopathic Pulmonary Fibrosis Based on Personalized Lung Poromechanical Modeling

Pulmonary function is tightly linked to the lung mechanical behavior, especially large deformation during breathing. Interstitial lung diseases, such as idiopathic pulmonary fibrosis (IPF), have an impact on the pulmonary mechanics and consequently alter lung function. However, IPF remains poorly understood, poorly diagnosed, and poorly treated. Currently, the mechanical impact of such diseases is assessed by pressure–volume curves, giving only global information. We developed a poromechanical model of the lung that can be personalized to a patient based on routine clinical data. The personalization pipeline uses clinical data, mainly computed tomography (CT) images at two time steps and involves the formulation of an inverse problem to estimate regional compliances. The estimation problem can be formulated both in terms of "effective", i.e., without considering the mixture porosity, or "rescaled," i.e., where the first-order effect of the porosity has been taken into account, compliances. Regional compliances are estimated for one control subject and three IPF patients, allowing to quantify the IPF-induced tissue stiffening. This personalized model could be used in the clinic as an objective and quantitative tool for IPF diagnosis. [DOI: 10.1115/1.4054106]

Manuscript received December 14, 2021; final manuscript received March 7, 2022; published online March 30, 2022. Assoc. Editor: David M. Pierce.

1 Introduction

Idiopathic pulmonary fibrosis (IPF) is a chronic pulmonary disease with a difficult diagnosis [1], severe prognosis [2,3], and limited treatment options [4]. It affects the pulmonary microstructure, with interstitial tissue scarring and thickening [5], leading to less efficient gas exchanges [6]. This also translates into an impact on the pulmonary mechanics: the lungs become stiffer, affecting their extensibility and thus their function [6]. As a consequence, IPF patients suffer from high breathlessness, which worsens with the disease evolution.

In addition to the mechanical impact of IPF on the lungs, mechanics is believed to have a major role in the disease progress [7]. Indeed, a mechanical vicious circle in place in IPF patients has been hypothesized: fibrosis induces higher stiffness and thus higher stresses (since the strain is imposed by the breathing function), which in turns activate the production of fibers by fibroblasts [5,8]. However, this vicious cycle remains hypothetical, and needs to be further studied—this paper is a first step toward an investigation of the role of mechanics in the progress of IPF through personalized biomechanical modeling.

Biomechanical modeling has already been used to help the diagnosis of various diseases such as myocardial infarction [9,10]. Addressing such applications requires patient-specific models, which have biophysical characteristics of the patients [11,12]. With respect to mechanical models, these characteristics are not only the geometric description of the organ but also the specific loading inducing organ deformations and the specific material behavior of the organ [13]. The patient attributes are usually derived from clinical data, such as medical imaging, pressures, or other relevant measurements [14].

Specifically for the lungs, several models and estimation procedures have been proposed in the literature. Various constitutive laws have been considered for the parenchyma, either based on micromechanics [15,16] or directly at the tissue scale [17]. Some such laws have been used within full organ scale models, mostly focusing on air flows and gas exchanges [18,19], although some models were used for detailed solid mechanics analysis [20,21]. However, Tawhai et al. [21] used an empirical compressible hyperelastic strain energy function not related to the tissue microstructure nor based on experimental measurements, which was used only to represent gross in vivo tissue behavior and whose parameters do not have a physical meaning. Berger et al. [20] used the same poromechanics foundation as the present work; however, various aspects of the model, such as the unloaded configuration and boundary conditions, which were not critical for the analysis, were defined in a purely mathematical manner, departing from physiology. Finally, in line with pure modeling approaches, existing personalized modeling approaches mostly focus on respiratory aspects [19,22].

We recently proposed a lung biomechanical model, based on a novel poromechanics behavior law, and specific boundary conditions [23–25]. The constitutive framework relies on the general formulation of poromechanics detailed in Ref. [26] and based on Refs. [27] and [28], describing the lung tissue as a mixture of "solid" (tissue & blood) and fluid (air). The boundary conditions contain the (negative) pleural pressure that inflates the lungs, and frictionless bilateral contact with the thorax. The model focuses on the end-exhalation and end-inhalation states (which are assumed to be at static equilibrium) and has been shown to adequately reproduce many elements of lung physiology [23,24].

In this paper, we introduce a personalization pipeline associated with the lung model. It is solely based on clinical data, namely, three-dimensional (3D) CT images, routinely acquired on IPF patients at the Avicenne APHP Hospital, Bobigny, which is one of two referral centers for rare pulmonary diseases in France. Patient-specific geometrical, kinematical, and physiological (i.e., local porosity and fibrosis state) information is directly extracted from the images by image processing. Mechanical information, i.e., regional tissue stiffness, is estimated through an inverse problem solved by a stochastic derivative-free algorithm. Several aspects of the personalization procedure are investigated, and then clinically relevant analyses are performed by applying the pipeline to one control subject and three IPF patients. By estimating the parenchymal tissue regional stiffness in health and disease, our personalized modeling pipeline could help better understand the role of mechanics in IPF progression, and better classify IPF patients.

The paper is organized as follows. In Sec. 2.1, we detail the clinical data that is routinely acquired on IPF patients and can be used to personalize a biomechanical model. Then, in Sec. 2.2, we briefly recall the main components of our pulmonary poromechanics model, which was fully detailed in Refs. [23] and [24]. In Sec. 2.3, we describe the personalization pipeline, which is the main technical novelty of this paper. In Sec. 2.4, we describe the synthetic data that will be used to validate the model and personalization procedure. The results section is split into three parts, focusing on validation based on synthetic (Sec. 3.1) and clinical (Sec. 3.2) data, followed by the first clinically relevant results obtained with our personalized modeling approach (Sec. 3.3). The paper ends with a discussion about the impact of various hypotheses and parameters of the model, its current limitations, and potential improvements (Sec. 4).

2 Materials and Methods

2.1 Clinical Data. Since the final aim of this work is to build a biomechanical model-based clinical tool, we only rely on routine clinical data. Even though a wide range of data is acquired in the clinic and stored in patients' medical records, not all data are directly usable in the context of the biomechanical model described in Sec. 2.2, and we focus on thoracic images only. Among the various techniques that can be used for in vivo lung imaging, including X-rays, computed tomography (CT) [29], magnetic resonance imaging [30], ultrasound [31], we use CT scans which are routinely performed for the diagnosis, classification, and monitoring of IPF patients, notably thanks to their high spatial and temporal resolution, and large field of view.

In this study, we used 3D CT scans of three IPF patients (selected for being highly representative of the disease) and one control subject (patient without pulmonary disease and normal thoracic scan), which were performed at the Avicenne APHP Hospital, Bobigny, France. Patients data were retrospectively retrieved according to the French law on medical research and compiled as required by the *Commission Nationale de l'Informatique et des Libertés* (CNIL; the French national data protection authority). The study not requiring an informed consent received authorization CLEA-2019-96 from the *Comité Local d'Éthique d'Avicenne* (CLEA).

Following latest recommendations [32], two 3D CT scans were performed on each subject, at end-exhalation and end-inhalation, allowing to capture not only the subject-specific lung geometry but also the breathing kinematics. Throughout the paper, images at end-exhalation are denoted by I_e, while images at end-inhalation are denoted by I_i. The scans were performed in the supine position, with the arms above the head and in breath-hold during image acquisition. Details on patients and images characteristics are reported in Table 1.

2.2 Lung Poromechanical Modeling. The lung poromechanical model used in this study has been described in detail in Refs. [23] and [24]. We only recall here the main points used in this work.

2.2.1 Poromechanical Framework

2.2.1.1 Poromechanics foundations. We propose to model the lungs as a two-phase porous continuum, where the solid phase corresponds to interstitial tissue and blood, and the fluid phase corresponds to the air present in airways and alveoli. To do so, we

Table 1 Characteristics of images used to personalize the model for each subject

Subject	Sex	Age (y)	Step	Voxel size (mm)	Image size (voxels)]
C1	M	72	E	$0.64 \times 0.64 \times 0.70$	$512 \times 512 \times 455$
			I	$0.72 \times 0.72 \times 0.70$	$512 \times 512 \times 455$
P1	M	67	E	$0.66 \times 0.66 \times 0.70$	$512 \times 512 \times 446$
			I	$0.66 \times 0.66 \times 0.70$	$512 \times 512 \times 446$
P2	M	61	E	$0.69 \times 0.69 \times 0.70$	$512 \times 512 \times 396$
			I	$0.69 \times 0.69 \times 0.70$	$512 \times 512 \times 396$
P3	F	66	E	$0.68 \times 0.68 \times 0.70$	$512 \times 512 \times 475$
			I	$0.62 \times 0.62 \times 0.70$	$512 \times 512 \times 423$

In the "subject" column, C and P stand for control and patient, respectively. In the "sex" column, F and M stand for female and male, respectively. In the "step" column, E and I stand for end-exhalation and end-inhalation, respectively.

use the mixture theory [27,28], specifically the formulation of Ref. [26], which is compatible with large strains as required by the pulmonary setting. Thus, the lung microstructure is characterized by the porosity, i.e., the volume fraction of air, which is denoted by Φ_{f0} in a given reference configuration (Ω_0, Γ_0), and ϕ_f in the deformed configuration (ω, γ). During lung deformation, fluid circulates in the mixture, as air enters the lungs during inhalation and goes out during exhalation. The added fluid mass per unit volume of the reference configuration is denoted by $\overline{\rho}_{f+}$.

2.2.1.2 Specific hypotheses. As in Ref. [26], the fluid is assumed to be incompressible, and the transformation is considered as isothermal. In addition to these general assumptions, we make the following two specific hypotheses: (i) the end-exhalation and end-inhalation states correspond to static equilibriums; and (ii) in these states the internal fluid pressure is homogeneous and equal to the atmospheric pressure, which is considered null here. Thus, the proposed model only describes the two equilibrium states of end-exhalation and end-inhalation, and not the path in between these states.

2.2.1.3 Kinematics. The transformation between the reference and deformed configurations is described by the mapping

$$\underline{\chi} := \begin{cases} \Omega_0 \to \omega \\ \underline{X} \mapsto \underline{x} = \underline{\chi}(\underline{X}) \end{cases} \tag{1}$$

The associated displacement field is $\underline{U}(\underline{X}) := \underline{\chi}(\underline{X}) - \underline{X}$, and the deformation gradient is $\underline{\underline{F}}(\underline{X}) := \underline{\underline{\nabla}}\,\underline{\chi} = \underline{\underline{1}} + \underline{\underline{\nabla}}\,\underline{U}$. The local volume change of the mixture is given by $J := \det(\underline{\underline{F}})$. The quantities $\Phi_s := (1 - \phi_f) \cdot J$ and $\Phi_f := \phi_f \cdot J$, such that $\Phi_f = J - \Phi_s$, are the contributions of the solid and the fluid phases to the mixture volume change. The right Cauchy-Green deformation tensor is denoted by $\underline{\underline{C}} := \underline{\underline{F}}^T \cdot \underline{\underline{F}}$, and its classical first three invariants are $I_1 := \mathrm{tr}(\underline{\underline{C}})$, $I_2 := (\mathrm{tr}(\underline{\underline{C}})^2 - \mathrm{tr}(\underline{\underline{C}}^2))/2$, and $I_3 := \det(\underline{\underline{C}}) = J^2$. Finally, the Green–Lagrange strain tensor is denoted by $\underline{\underline{E}} := (\underline{\underline{C}} - \underline{\underline{1}})/2$. These quantities are represented in Fig. 1.

2.2.1.4 Equilibrium. We write the global equilibrium of the mixture in weak form, i.e., under the form of the principle of virtual work. Depending on the problem, it can be formulated on the deformed configuration ω, in terms of the Cauchy stress tensor $\underline{\underline{\sigma}}$

$$\int_\omega \underline{\underline{\sigma}} : \underline{\underline{\varepsilon}}(\underline{u}^*)\mathrm{d}\omega = W_{\mathrm{ext}}(\underline{u}^*) \quad \forall \underline{u}^* \tag{2}$$

where $\underline{\underline{\varepsilon}}(\underline{u}^*) := (\underline{\underline{\nabla}}\,\underline{u}^*)_{\mathrm{sym}}$ is the symmetric gradient of the displacement, i.e., the linearized strain tensor, or on the reference configuration Ω_0, in terms of the second Piola–Kirchhoff stress tensor $\underline{\underline{\Sigma}}$

$$\int_{\Omega_0} \underline{\underline{\Sigma}} : \mathrm{d}_{\underline{U}}\underline{\underline{E}} \cdot \underline{U}^* \mathrm{d}\Omega_0 = W_{\mathrm{ext}}(\underline{U}^*) \quad \forall \underline{U}^* \tag{3}$$

where $\mathrm{d}_{\underline{U}}\underline{\underline{E}} \cdot \underline{U}^*$ is the differential of the Green–Lagrange strain tensor. In both expressions, W_{ext} represents the virtual work of external forces, which will be detailed later.

A key point of the poromechanics framework is to add another equilibrium condition, local, between the fluid pressure, denoted by p_f, and the hydrostatic pressure in the solid (associated with solid volume change, as formally defined later), denoted by p_s [26–28]

$$p_f = p_s \tag{4}$$

2.2.2 Constitutive Framework

2.2.2.1 Mixture behavior. Following Ref. [26], and as detailed in Refs. [23] and [24], the Helmholtz free energy of the mixture $\overline{\psi}$ is decomposed into solid and fluid parts

$$\overline{\psi}(\underline{\underline{E}}, \overline{\rho}_{f+}) = \overline{\psi}_s(\underline{\underline{E}}, \Phi_s) + \overline{\psi}_f(\Phi_f) \tag{5}$$

where $\overline{\psi}_s$ and $\overline{\psi}_f$ are the free energies of the solid and the fluid phase, respectively. Since the second Piola–Kirchhoff stress tensor $\underline{\underline{\Sigma}}$ derives from $\overline{\psi}$, we have

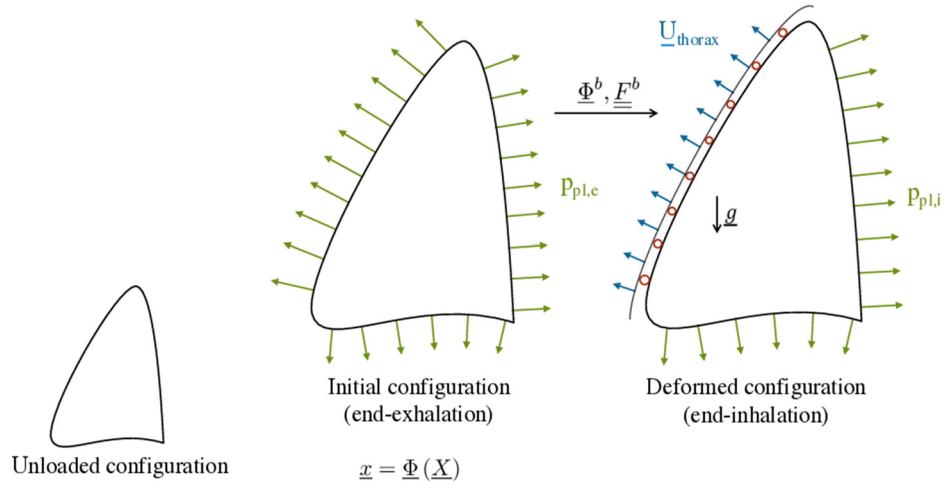

Fig. 1 Schematic representation of the main quantities describing the system and the boundary conditions considered in the mechanical problem

$$\underline{\underline{\Sigma}} = \frac{\partial \overline{\psi}(\underline{\underline{E}}, \overline{p}_{f+})}{\partial \underline{\underline{E}}} = \frac{\partial \overline{\psi}_s}{\partial \underline{\underline{E}}} - p_s J \underline{\underline{C}}^{-1} \tag{6}$$

where $p_s := -\frac{\partial \overline{\psi}_s}{\partial \Phi_s}$ represents the part of the solid hydrostatic pressure associated with volume change.

2.2.2.2 Solid effective behavior. The following decomposition of the solid free energy $\overline{\psi}_s$ is considered as proposed in Ref. [26]:

$$\overline{\psi}_s(\underline{\underline{E}}, \Phi_s) = \overline{W}_{skel}(\underline{\underline{E}}) + \overline{W}_{bulk}(\Phi_s) \tag{7}$$

where $\overline{W}_{skel}(\underline{\underline{E}})$ is the free energy of the solid considered as a structure and $\overline{W}_{bulk}(\Phi_s)$ accounts for the compressibility of the solid phase. We consider the following energies as proposed in Refs. [23] and [24]:

$$\begin{cases} \overline{W}_{skel}(\underline{\underline{E}}) = \overline{\alpha}\left(e^{\delta\left(J^2-1-2\ln(J)\right)} - 1\right) \\ \qquad\qquad + \overline{\beta}_1(I_1 - 3 - 2\ln(J)) + \overline{\beta}_2(I_2 - 3 - 4\ln(J)) \\ \overline{W}_{bulk}(\Phi_s) = \overline{\kappa}\left(\dfrac{\Phi_s}{1-\Phi_{f0}} - 1 - \ln\left(\dfrac{\Phi_s}{1-\Phi_{f0}}\right)\right) \end{cases}, \tag{8}$$

where $\overline{\alpha}, \overline{\beta}_1, \overline{\beta}_2, \delta, \overline{\kappa}$ are material parameters. $\overline{\kappa}$ is the solid bulk modulus, which should be taken large with respect to the shear modulus to ensure quasi-incompressibility of the solid part. These parameters represent the effective behavior of the solid part of the mixture, which depends on the porosity of the mixture.

2.2.2.3 Solid rescaled behavior. In order to introduce, in the simplest possible way, the porosity dependency into the mixture behavior, we define the following rescaling of the effective energy using the reference porosity:

$$\overline{\psi}_s = (1 - \Phi_{f0})\widetilde{\psi}_s \tag{9}$$

which leads to

$$\begin{cases} \overline{W}_{skel}(\underline{\underline{E}}) = (1 - \Phi_{f0})\widetilde{W}_{skel}(\underline{\underline{E}}) \\ \overline{W}_{bulk}(\Phi_s) = (1 - \Phi_{f0})\widetilde{W}_{bulk}(\Phi_s) \end{cases} \tag{10}$$

where $\widetilde{\psi}_s$, $\widetilde{W}_{skel}$, and $\widetilde{W}_{bulk}$ are the rescaled free energies per unit solid mass, corresponding to the effective free energies $\overline{\psi}_s$, $\overline{W}_{skel}$, and $\overline{W}_{bulk}$, respectively. The effective mechanical parameters $\overline{\theta}$ and the rescaled mechanical parameters $\widetilde{\theta}$ are then linked by

$$\overline{\theta} = (1 - \Phi_{f0})\widetilde{\theta} \quad \forall \overline{\theta} \in \{\overline{\alpha}, \overline{\beta}_1, \overline{\beta}_2, \overline{\kappa}\} \tag{11}$$

The parameter δ remains the same in both effective and rescaled behaviors since it describes the nonlinear part of the energy. Nevertheless, using these rescaled potentials, the mixture can be fully heterogeneous (which has been shown to allow for a better fit of ex vivo experimental measurements [33]) even with homogeneous material parameters, as long as the porosity is heterogeneous.

2.2.2.4 Compliance measure. For the compliance analysis, we need a quantity that is independent from the chosen constitutive behavior, so we define the global compliance between two time points t_0 and t_1 as the volume change divided by the pressure change

$$C_{t_0 \to t_1} = \frac{V_{t_1} - V_{t_0}}{p_{pl,t_1} - p_{pl,t_0}} \tag{12}$$

In the rest of the paper, we will denote by C the compliance between the end-exhalation and end-inhalation states for a normal breathing at rest, i.e., when the pleural pressure values are 0.5 kPa and 0.8 kPa, respectively.

2.2.3 Poromechanical Formulation. As illustrated in Fig. 1, the initial configuration corresponds to the end-exhalation configuration and the deformed configuration to the end-inhalation configuration. Since the constitutive behavior of the solid phase is nonlinear and the initial configuration is loaded, the unloaded configuration has to be determined. Thus, the computation of breathing from the initial to the deformed configuration has to be performed in two steps:

Step 1: First, the computation of the unloaded configuration from the initial configuration, which allows to deduce the reference porosity field and the initial stress field;
Step 2: Then, the computation of the deformed configuration knowing the unloaded configuration.

2.2.3.1 From the end-exhalation to the unloaded configuration. Step 1 is an inverse problem which is fully described in Refs. [23] and [24]. The boundary conditions used for this step are only the negative pleural pressure on the whole surface of the lung. Rigid body motions are also blocked by applying the "3-2-1 method" on the three nodes defining the most orthogonal trihedron in the mesh: the origin is blocked in all three directions, the first node in the second and third directions, and the second node in the third direction. The weak formulation of the problem is

$$\text{Find } (\underline{u}_0, \phi_{f0}), \begin{cases} \forall \underline{u}^*, \displaystyle\int_{\omega_e} \underline{\underline{\sigma}}(\underline{u}_0, \phi_{f0}) : \underline{\underline{\varepsilon}}(\underline{u}^*) d\omega = -\int_{\gamma_e} p_{pl,e}\, \underline{n} \cdot \underline{u}^* d\gamma \\ \forall \underline{x},\ p_f = -\dfrac{\partial \overline{W}_{bulk}}{\partial \Phi_s}(\underline{u}_0, \phi_{f0}) \end{cases} \tag{13}$$

where a change of variable has been performed (the unknown is the inverse displacement $\underline{u}_0$, or equivalently the inverse mapping $\underline{\chi}_0^{-1}$, associated with the deformation gradient $\underline{\underline{f}}_0 := \underline{\underline{\nabla}}\, \underline{\chi}_0^{-1} = \underline{\underline{1}} + \underline{\underline{\nabla}}\, \underline{u}_0$ and the volume change $j_0 := \det \underline{\underline{f}}_0$), as originally proposed in Ref. [34]. The Cauchy stress tensor is here defined as $\underline{\underline{\sigma}}(\underline{u}_0, \phi_{f0}) = j_0 \underline{\underline{f}}_0^{-1} \cdot (\underline{\underline{\Sigma}}(\underline{u}_0, \phi_{f0}) \circ \underline{\chi}_0^{-1}) \cdot \underline{\underline{f}}_0^{-T}$, where the second Piola–Kirchhoff stress tensor is given by $\underline{\underline{\Sigma}}(\underline{u}_0, \phi_{f0}) = \frac{\partial \overline{W}_{skel}}{\partial \underline{\underline{E}}}(\underline{u}_0, \phi_{f0}) - p_s(\underline{u}_0, \phi_{f0}) J_0 \underline{\underline{C}}_0^{-1}$ with $p_s(\underline{u}_0, \phi_{f0}) = -\frac{\partial \overline{W}_{bulk}}{\partial \Phi_s}(\underline{u}_0, \phi_{f0})$.

2.2.3.2 From the unloaded to the end-inhalation configuration. The boundary conditions in Step 2 are more complex since breathing involves a complex environment (pleura, diaphragm, intercostal muscle, etc.). In addition to the negative pleural pressure on the whole surface of the lung, a bilateral contact between the lung surface and the thorax surface is considered. This contact is assumed to be frictionless and with no separation of the surfaces in contact. The thorax displacement is also taken into account.

Under the previously mentioned hypotheses, the lung poromechanical behavior is described by the following system:

$$\text{Find } (\underline{U}, \Phi_f) \begin{cases} \forall \underline{U}^*, \displaystyle\int_{\Omega_0} \frac{\partial \overline{W}_{skel}}{\partial \underline{\underline{E}}} : d_{\underline{U}} \underline{\underline{E}} \cdot \underline{U}^* d\Omega_0 - \int_{\Omega_0} p_f J \underline{\underline{C}}^{-1} : d_{\underline{U}} \underline{\underline{E}} \cdot \underline{U}^* d\Omega_0 \\ \qquad\qquad = -\displaystyle\int_{\Gamma_0} p_{pl} J \left(\underline{\underline{F}}^{-T} \cdot \underline{N}_0\right) \cdot \underline{U}^* d\Gamma_0 \\ \forall \underline{X},\ p_f = -\dfrac{\partial \overline{W}_{bulk}}{\partial \Phi_s} \end{cases} \tag{14}$$

The first equation corresponds to the global mechanical equilibrium of the pulmonary mixture, i.e., Eq. (3). Note that here the

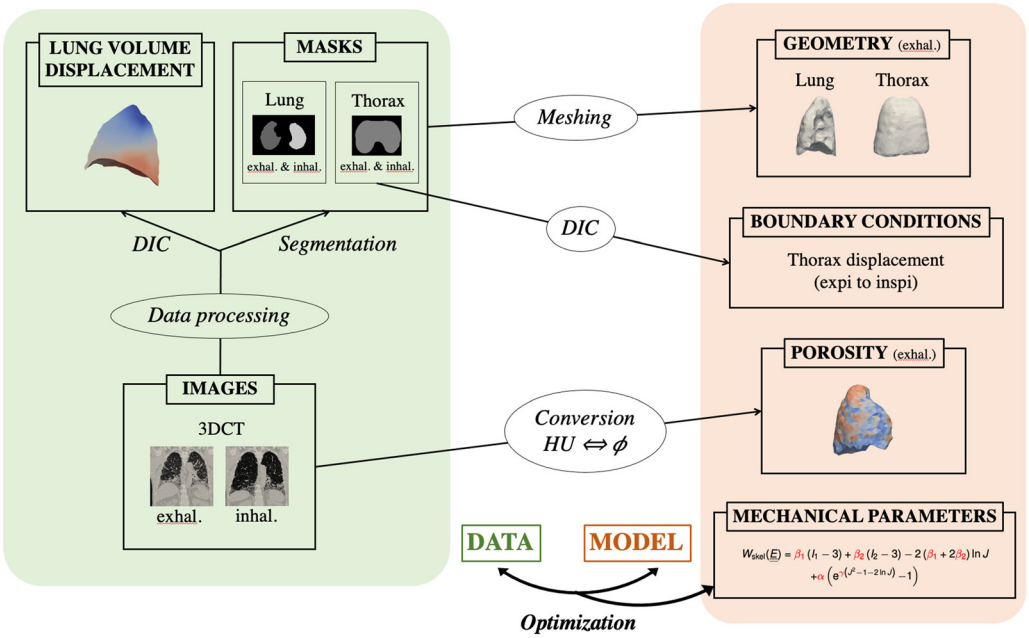

Fig. 2 Summary of the personalization pipeline. (DIC = digital image correlation. HU = Hounsfield units.)

fluid pressure p_f is known, taken as zero (atmospheric pressure) in our case.

2.2.4 Implementation. The computation of the reference configuration (step 1 of the direct problem) has been implemented using the FEniCS library [35,36]. Step 2 is computed with ABAQUS.[1] The contact is defined as a master-slave, finite sliding, and node-to-surface. The master surface and the slave surface, i.e., the thorax surface and the lung surface, respectively, are adjusted at the start of the simulation to remove gaps and overlaps.

2.3 Model Personalization. Using the clinical data described in Sec. 2.1, several components of the poromechanical model described in Sec. 2.2 can be personalized for a given subject. We now describe the personalization of the lung and thorax geometries, the disease extent, the thorax motion, and material parameters, namely, the porosity field and one regional compliance parameter. The whole model personalization pipeline is illustrated in Fig. 2.

2.3.1 Geometry. As described in Sec. 2.2, the proposed lung model requires two finite element meshes: a volume mesh for the lungs, and a surface mesh for the thorax, which is used to define proper boundary conditions for the lungs. Patient-specific meshes are obtained from the clinical images described in Sec. 2.1 as follows.

2.3.1.1 Lung geometry. For each subject, the lungs are segmented on the end-exhalation images (I_e), leading to a binary mask denoted by $M_{l,e}$. This is performed using the algorithm described in Ref. [29], which is specifically developed for the segmentation of fibrotic lungs. Indeed, if in CT images healthy lungs are easily distinguishable from their surroundings (because the contrast in air/water content, and thus in image intensity, is high), it is not the case for lungs with fibrotic regions, for which the image intensity contrast with the surrounding can be very low. One example mask is shown in Fig. 3.

Then, a finite element mesh is generated from the segmentation. To do so, the lung surface is extracted from the lung mask using MEVISLAB [37], and is used to generate a surface mesh and then a volume mesh using GMSH [38,39].

2.3.1.2 Thorax geometry. For the rib cage finite element geometry, only a surface mesh is required. For each subject, the rib cage is manually segmented using MEVISLAB on the same end-exhalation image I_e as the lung, leading to another binary mask denoted by $M_{t,e}$, with special care to generate a rib cage surface matching with the lung surface in the contact area between the rib cage and the lung. The thorax surface is then extracted using MEVISLAB, and a surface finite element mesh is generated using GMSH [38,39].

2.3.2 Thorax Motion. In the model, the thorax surface motion is prescribed. It can be extracted from the clinical images described in Sec. 2.1 as follows. For each subject, a binary mask of the thorax at end-inhalation, denoted by $M_{t,i}$, is generated following the same procedure as the binary mask of the thorax at end-exhalation $M_{t,e}$. A displacement field between the two masks is computed using the finite element motion tracking tool described in Ref. [40], using a small hyperelastic regularization to prevent convergence issues induced by the ill-posedness of the shape tracking problem. This displacement field is then projected onto the thorax surface finite element mesh.

2.3.3 Porosity Field. Porosity information can be computed from CT images [41]. Indeed, CT measures the attenuation of X-rays by tissue, and hence, the contrast in CT images comes from a difference in tissue density. CT image pixels are displayed according to the mean attenuation of the tissue volume that they represent formulated in the Hounsfield units (HU) scale. Typically, water and air have an attenuation of 0 HU and −1000 HU, respectively.

Considering a linear variation of porosity with HU, the local porosity can be computed for each pixel with the following expression:

$$\phi_f(\underline{x}) = \frac{\mathrm{HU}(\underline{x}) - \mathrm{HU}_{\mathrm{tissue}}}{\mathrm{HU}_{\mathrm{air}} - \mathrm{HU}_{\mathrm{tissue}}} \tag{15}$$

with $\mathrm{HU}_{\mathrm{tissue}} = 0\,\mathrm{HU}$ considering that biological tissues are mainly composed of water and $\mathrm{HU}_{\mathrm{air}} = -1000\,\mathrm{HU}$.

Thus, for each subject, the porosity field from the end-exhalation image I_e is projected onto the lung finite element mesh. For each element, the porosity is taken constant, and equal to the mean of the pixel values for all the pixels lying inside the element.

[1] https://www.3ds.com/products-services/simulia/products/abaqus

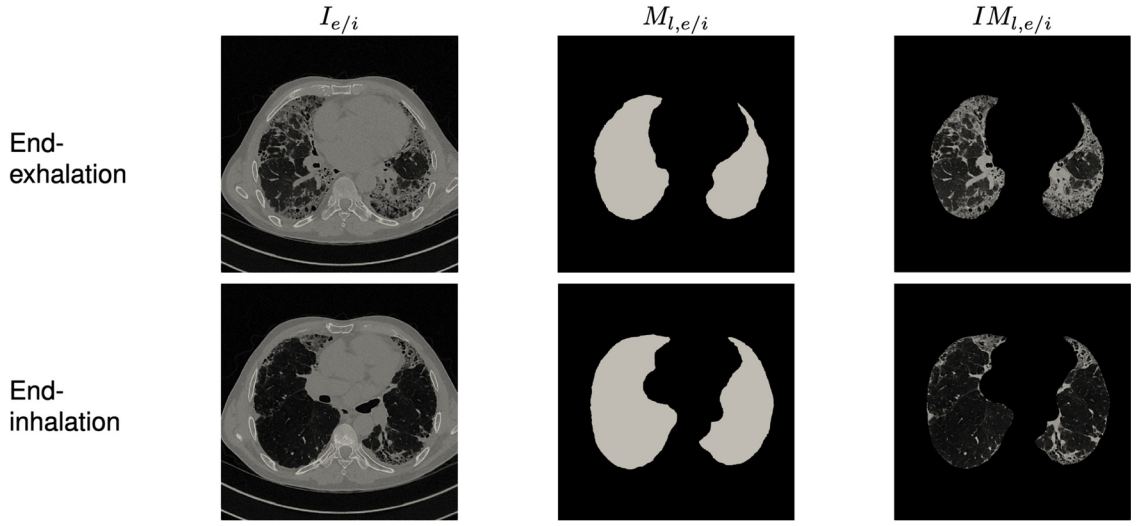

Fig. 3 Visualization of the different images used in the whole process of image registration. *I* are the raw images, M_l are the binary images computed by the segmentation of lungs on *I*, IM_l are the multiplication between *I* and M_l. The first step of the image registration consists in correlating lung shape between $M_{l,e}$ and $M_{l,i}$. Then lung volume is correlated during the second step using $IM_{l,e}$ and $IM_{l,e}$

This projection is performed using VTK,[2] as described in details in Ref. [10]. And thanks to this heterogeneous porosity field, in the rescaled parameters formulation, the mixture behavior is actually fully heterogeneous even when considering homogeneous material parameters.

2.3.4 Healthy and Diseased Regions. In the CT images, the lung regions affected by IPF are denser and thus brighter than healthy regions. For all patients, these fibrotic regions are manually segmented in the end-exhalation image I_e using ITK-SNAP [42], and the segmentation is validated by a radiologist. Then, this segmentation is projected onto the lung finite element mesh. For each element, if more than half the pixels lying inside the element are fibrotic then the element is considered fibrotic, otherwise it is considered healthy. Eventually, the mesh is composed of two binary regions, i.e., the healthy and diseased regions.

2.3.5 Regional Compliance

2.3.5.1 Estimation problem general formulation. Patient-specific mechanical parameters of the skeleton energy $\overline{W}_{\text{skel}}$ are estimated using the above lung poromechanical model and clinical data. This inverse problem is formulated as an optimization problem, in which the solution is the set of mechanical parameters Θ minimizing a cost function f, characterizing the distance between the model and the data. Thus, the model best fits the data for the set of parameters Θ, solution of the optimization problem. Two different cost functions are investigated, differing by the nature of the considered data: the first one is based on displacement fields that can be extracted from the images, as described in the next paragraph, while the second one is based on the images directly.

2.3.5.2 Lung Motion Tracking. In order to provide an image-based estimation of the displacement field of the lungs between end-exhalation and end-inhalation, denoted by $\underline{U}_{\text{DIC}}$, we employ the finite element digital image correlation (DIC) method detailed in Refs. [40] and [43]. However, thoracic image registration involves several difficulties [44–46], including the very large breathing displacements (as the lung base is pulled by the diaphragm by several centimeters), and the displacement discontinuity at the border (as the lung is sliding against the thorax). Thus, for each subject the lung motion tracking is performed in multiple steps:

(1) A binary mask of the lungs at end-inhalation, denoted by $M_{l,i}$, is generated following the same procedure as the binary mask of the lungs at end-exhalation $M_{l,e}$.
(2) A finite element mesh is created from the binary mask at end-exhalation $M_{l,e}$, including a layer of elements lying outside the mask.
(3) The displacement between the masks at end-exhalation $M_{l,e}$ and end-inhalation $M_{l,i}$ is computed, following [40] and including a very small hyperelastic regularization term [47] to prevent convergence issues induced by the ill-posedness of the shape registration problem. It corresponds to the displacement of the lung shape, and is denoted by $\underline{U}_{\text{shape}}$. During this process, the mesh layer ensures that voxels on both sides of the mask border are considered, so that the border motion is well tracked.
(4) Two masked images, denoted by $IM_{l,e}$ and $IM_{l,i}$, are computed as the multiplication of the CT image $I_{e/i}$ and the binary masks $M_{l,e/i}$, so that pixels inside the lungs are textured as in the CT image and pixels outside the lungs have zero intensity.
(5) The displacement between the masked images at end-exhalation $IM_{l,e}$ and end-inhalation $IM_{l,i}$ is computed, following [40] and including an equilibrium gap regularization term [48] to impose that the tracked displacement field be compatible with mechanical equilibrium. It corresponds to the estimated lung displacement $\underline{U}_{\text{DIC}}$. For this process, the displacement field $\underline{U}_{\text{shape}}$ is used as an initial guess, making the tracking robust.

$I_{e/i}$, $M_{l,e/i}$, and $IM_{l,e/i}$ can be seen in Fig. 3, both for end-exhalation and end-inhalation. The registration process is done for each lung separately.

2.3.5.3 Cost function based on displacement fields. The first cost function considered to estimate compliance parameters corresponds to the finite element model updating (FEMU) approach [49–51] and relies on displacement fields computed through motion tracking. It compares the displacement field $\underline{U}(\theta)$ computed with the model for a given set of parameters θ with the displacement field $\underline{U}_{\text{DIC}}$ computed by image registration. It corresponds to the following expression:

$$f_{\text{disp}}(\theta) := \frac{\|\underline{U}(\theta) - \underline{U}_{\text{DIC}}\|_{L^2}}{\|\underline{U}_{\text{DIC}}\|_{L^2}} \tag{16}$$

[2] http://www.vtk.org

Table 2 Model parameters used in simulations, with either the effective parameters or the rescaled parameters

			Simulations with effective parameters	Simulations with rescaled parameters
Material	$\overline{\beta}_1$	(kPa)	0.1	—
	$\overline{\beta}_2$	(kPa)	0.2	—
	$\widetilde{\beta}_1$	(kPa)	—	0.2
	$\widetilde{\beta}_2$	(kPa)	—	0.4
	δ	(–)	0.5	0.5
Loading	p_{f}	(kPa)	0.00	
	$p_{\mathrm{pl,e}}$	(kPa)	−0.50	
	$p_{\mathrm{pl,i}}$	(kPa)	−1.85	

The parameters are the effective parameters $\overline{\theta} = \{\overline{\beta}_1, \overline{\beta}_2, \delta\}$ of the solid free energy $\overline{\psi}_{\mathrm{s}}$, or the rescaled parameters $\widetilde{\theta} = \{\widetilde{\beta}_1, \widetilde{\beta}_2, \delta\}$ of the solid free energy $\widetilde{\psi}_{\mathrm{s}}$, as well as the fluid pressure p_{f} (which is zero according to the free breathing assumption), the end-exhalation pleural pressure $p_{\mathrm{pl,e}}$, the end-inhalation pleural pressure $p_{\mathrm{pl,i}}$.

2.3.5.4 Cost function based on images. The second considered cost function corresponds to an integrated image correlation approach [52,53] and relies on the images themselves. It is composed of two terms weighted by the factor k

$$f_{\mathrm{imag}}(\theta) := f_{\mathrm{reg}}(\theta) + k f_{\mathrm{shape}}(\theta) \tag{17}$$

where

$$f_{\mathrm{reg}}(\theta) := \frac{\| M_{l,e} M_{l,i} \left(I_i \circ \underline{\chi}(\theta) - I_e \right) \|_{L^2}}{\| M_{l,e} M_{l,i} I_e \|_{L^2}} \tag{18}$$

is the same energy that is minimized during image registration, comparing image intensities, and $f_{\mathrm{shape}}(\theta)$ quantifies the similarity between the computed and the measured end-inhalation shapes, which is needed mainly for fibrosis cases. Indeed, as was already mentioned, the fibrotic parts and lung surroundings have a similar image intensity. Thus, the lung shape resulting from the estimation process tends to be overinflated. The shape term is computed using the Dice coefficient [54] between two binary images, $M_{l,i}$ coming from the lung segmentation of I_i and $M_{l,i,\mathrm{model}}(\theta)$ masking I_i with the deformed mesh surface computed with the model for a given set of parameters θ, and is defined as

$$f_{\mathrm{shape}}\left(M_{l,i}, M_{l,i,\mathrm{model}}(\theta)\right) := \frac{2TP}{2TP + FP + FN} \tag{19}$$

where TP, FP, and FN are the true positives, the false positives, and the false negatives, respectively. In the image registration term f_{reg}, the use of the factor $M_{l,e}M_{l,i}$ implies that only the pixels corresponding to the lung area are taken into account, which makes f_{reg} independent from the surrounding area of the image. Computing the cost function f_{imag} using unmasked or masked images will then lead to the same value. The choice of the weight factor k is made in such a way as to balance the variation of each term of f_{imag}.

2.3.5.5 Estimated Parameters. Either the effective parameters $\{\overline{\alpha}, \overline{\beta}_1, \overline{\beta}_2, \delta\}$ or the rescaled parameters $\{\widetilde{\alpha}, \widetilde{\beta}_1, \widetilde{\beta}_2, \delta\}$ can be estimated: the estimation of the rescaled parameters requires a porosity field Φ_{f0} contrary to the estimation of the effective parameters. However, the estimation of four parameters with such data (images at only two different time steps, with essentially a surface pressure loading) is highly ill-posed. Consequently, only the main stiffness parameters, $\widetilde{\Theta} = \{\widetilde{\alpha}\}$ or $\overline{\Theta} = \{\overline{\alpha}\}$, are estimated and the others are set. The parameters are taken homogeneous by regions, which are defined as sets of elements. In this study, the lung is considered as composed of either one or two regions, typically to represent healthy and fibrotic tissues, but there is no restriction to consider more than two regions.

2.3.5.6 Implementation. The optimization process is solved using the stochastic derivative-free numerical optimization algorithm CMA-ES [55,56], which evaluates the direct problem several times with different sets of parameters. For each evaluation of the direct problem, a set of parameters is considered and both steps described in Sec. 2.2 are computed, i.e., the computation of the unloaded configuration and the computation of the deformed configuration. At each iteration, the evaluations of the cost function are performed in parallel.

2.4 Synthetic Data. In order to validate the mechanical parameters estimation, which corresponds to the material part of the model personalization, we generate synthetic data for both model parametrizations (i.e., effective and rescaled parameters) and both cost functions (i.e., displacement-based and image-based). These synthetic data are based on the model of subject P1. All ingredients of the model are fixed: the lung and thorax geometries, the partition into healthy and diseased regions, the material parameters and the porosity, the thorax displacement, and the pleural pressure.

2.4.1 Synthetic Displacements. First, a synthetic displacement field, denoted by $\underline{U}_{\mathrm{DIC,synth}}$, is generated by simply running the model. It will be used as synthetic data for the validation of the displacement-based f_{disp} cost function.

2.4.2 Synthetic Images. Then, using the same simulation, two synthetic images are generated: an initial image $I_{e,\mathrm{synth}}$ and a deformed image $I_{i,\mathrm{synth}}$, corresponding to the end-exhalation and the end-inhalation configurations, respectively. They will be used as synthetic data for the validation of the image-based f_{imag} cost function. The intensity field of $I_{e,\mathrm{synth}}$ is defined as

$$I_{e,\mathrm{synth}}(\underline{x}) = \begin{cases} 0 & \text{if } \underline{x} \notin \Omega \\ \left| \sin \dfrac{\pi x_0}{s} \right| \left| \sin \dfrac{\pi x_1}{s} \right| \left| \sin \dfrac{\pi x_2}{s} \right| & \text{if } \underline{x} \in \Omega \end{cases} \tag{20}$$

with x_0, x_1, x_2 the three spatial coordinates of $\underline{x}$ and $s = 1/3$ cm the tagging period. This is the simplest model of tagged magnetic resonance imaging, which we use here for its good tracking properties [57]. Such an intensity field means that the image is textured only in the lung volume. The intensity field of $I_{i,\mathrm{synth}}$ is defined as

$$I_{i,\mathrm{synth}}(\underline{x}) = I_{e,\mathrm{synth}}(\underline{\chi}_{\mathrm{synth}}(\underline{x})) \tag{21}$$

where $\underline{\chi}_{\mathrm{synth}}$ is the transformation associated with the synthetic displacements $\underline{U}_{\mathrm{DIC,synth}}$.

3 Results

In this section, we present results based on both synthetic and clinical data. All the simulations are performed under the free breathing assumption ($p_{\mathrm{f}} = 0$) since all subjects studied were breathing freely. Unless specific values are mentioned in the following paragraphs, the model parameters used in the simulations are presented in Table 2.

Table 3 Synthetic validation of the estimation process with both criteria (displacement-based f_{disp} and image-based f_{imag}) and both effective and rescaled parameters

			f_{disp}		f_{imag}	
		Θ_{synth}	Θ_{estim}	Error (%)	Θ_{estim}	Error (%)
Effective	$\bar{\alpha}_h$	0.052	0.0520	3.7×10^{-4}	0.0520	-1.2×10^{-2}
	$\bar{\alpha}_l$	0.052	0.0520		0.0520	
	$\bar{\alpha}_d$	0.67	0.6700	-1.5×10^{-5}	0.6702	2.7×10^{-2}
Rescaled	$\tilde{\alpha}_h$	0.09	0.0910	1.1	0.0910	1.1
	$\tilde{\alpha}_d$	0.62	0.6200	3.9×10^{-3}	0.6200	2.3×10^{-4}

$\bar{\alpha}_h$ and $\tilde{\alpha}_h$ are the effective and rescaled parameters of the healthy region, respectively, whereas $\bar{\alpha}_d$ and $\tilde{\alpha}_d$ characterize the diseased region. Θ_{synth} are the parameters chosen to create the synthetic data as explained in Sec. 2.4. Θ_{estim} are the estimated parameters, resulting from the optimization algorithm explained in Sec. 2.3.5. The error between the synthetic parameters and the estimated parameters is computed as $(\Theta_{estim} - \Theta_{synth})/\Theta_{synth}$.

3.1 Verification and Analysis Based on Synthetic Data. This section focuses on results with synthetic data, as described in Sec. 2.4. The personalized model of the subject P1 is used (geometry, boundary conditions, and porosity). However, the data used in the estimation pipeline, either lung displacements or images, is synthetic.

3.1.1 Regional Compliances Identifiability. We first validate the estimation process with synthetic data for which exact material parameters are known. Such synthetic data are generated as described in Sec. 2.4: parameters are set, then the resulting displacement field is computed through the direct problem (data used with the displacement-based cost function f_{disp}) and an initial image is generated and deformed based on this displacement field to generate the deformed image (data used with the image-based cost function f_{imag}). More specifically, the model components of the subject P1 are used: lung and thorax geometries, thorax displacement, porosity field, and disease segmentation. Two datasets are generated, with effective and rescaled parameters, respectively. The model parameters concerning the pressure loading or the fixed material parameters are those presented in Table 2. The parameters that were used to generate the synthetic data and that are estimated are reported as Θ_{synth} in Table 3.

The validation is performed for both cost functions, displacement-based and image-based, as well as for both types of parameters, effective and rescaled. The results are presented in Table 3. Among all the cases, the error in the parameter value is at most 1%. The synthetic parameters are then well estimated using the CMA-ES algorithm, for both cost functions and both types of parameters.

3.1.2 Pleural Pressure Approximation. The patient-specific pleural pressure is not measured in our study. As a consequence, a generic inhalation pressure of $-1.85\,\text{kPa} \approx -18.6\,\text{cmH}_2\text{O}$, chosen in the physiological range, is used for all patients and the results of the parameter estimation are relative to this value. This is why the impact of the pleural pressure uncertainty on the compliance is investigated in this section. To that purpose, we consider the same synthetic data as in Sec. 3.1.1 for which the end-inhalation pleural pressure $p_{pl,i,synth}$ is known ($p_{pl,i,synth} = -1.85\,\text{kPa} \approx -18.6\,\text{cmH}_2\text{O}$). Then, we estimate the material parameters using this data and a model where the only change is the end-inhalation pleural pressure $p_{pl,i}$, which is different from $p_{pl,i,synth}$. The four cases considered have the following values for the end-inhalation pleural pressure: $p_{pl,i} = \lambda p_{pl,i,synth}$ with $\lambda \in \{0.8, 0.9, 1.1, 1.2\}$. The material parameters are estimated with the displacement-based cost function f_{disp} for both effective and rescaled parameters.

The results of the four cases studied are presented in Fig. 4. The regional pressure–volume curves for each pressure value are shown in the left plots; in the right plots, the regional compliance error as well as the compliance ratio (diseased compliance over healthy compliance) error are plotted as a function of λ, for each type of parameter.

The compliance is underestimated when the pressure is overestimated (which is consistent with the fact that we consider a higher pressure for the same deformation), and vice versa, for both effective and rescaled parameters. Moreover, the compliance error is larger in the diseased region (which is stiffer) than in the healthy region (which is less stiff). However, the compliance error is reduced when considering rescaled parameters compared to effective parameters.

The compliance ratio is also impacted by the pressure in the model, for both effective and rescaled parameters. Indeed, we see an underestimation of the compliance ratio when the pressure is itself underestimated, and vice versa. However, the error on the compliance ratio is reduced compared to the error on the compliances themselves.

3.1.3 Effective Versus Rescaled Potentials. In order to investigate the error induced by the use of effective potentials, which basically neglect the porosity variations within the lung regions, we use the synthetic data generated with rescaled potentials (which thus take into account the local porosities of the lung), and estimate effective parameters using the displacement-based cost function f_{disp}. The resulting optimized cost function is 3.75%, which is rather small compared to the errors obtained with in vivo data (17–23%, see Sec. 3.2). This result reflects that the porosity is quite homogeneous in each region, and that the porosity heterogeneity, mainly located at the interface between regions, does not impact the compliance estimation results significantly.

3.2 Validation and Analysis Based on Clinical Data. This section presents results with clinical data from one control and three diseased subjects, as described in Sec. 2.1.

3.2.1 Effective Versus Rescaled Potentials. We start by comparing the results obtained with effective and rescaled parameters. Both computations are performed for each subject and each cost function. Since there is no ground truth associated with this data, we compare the optimized cost function value, i.e., the fit between the estimated model and the data. The normalized difference between the optimal cost function value using rescaled parameters compared to the optimal cost function value using effective parameters is presented in Table 4.

For subjects C1 and P1, using rescaled parameters (thus taking into account local variations of porosity within lung regions) allows the optimized model to better fit the data, using both displacement-based and image-based cost functions. For subjects P2 and P3, it is the opposite: effective parameters allow for a better fit.

3.2.2 Displacement Versus Image CRITERIA. Another question raised in this work is the comparison between displacement-based and image-based criteria. Thus, for each subject and each type of parameters (effective versus rescaled), we now compare the compliance estimated from displacement data and the compliance estimated from image data. For the patients, we estimated both the global compliance (i.e., one zone) and the regional compliances (i.e., two zones, healthy versus diseased).

The results are represented in a Bland–Altman plot, shown in Fig. 5. The difference between compliances estimated based on both criteria is plotted as a function of the mean compliance. The bias in the difference between compliances is 0.04 ± 0.21 L/kPa, which means that in average the image-based criterion f_{imag} gives a slightly higher compliance than the displacement criterion f_{disp}. However, the bias is small compared to other error sources, and can be neglected. Consequently, both criteria can be considered to be equivalent.

3.2.3 Physiological Versus Arbitrary Disease Segmentation. We now investigate the impact of disease segmentation on the model-data fit. To do so, we define arbitrary disease

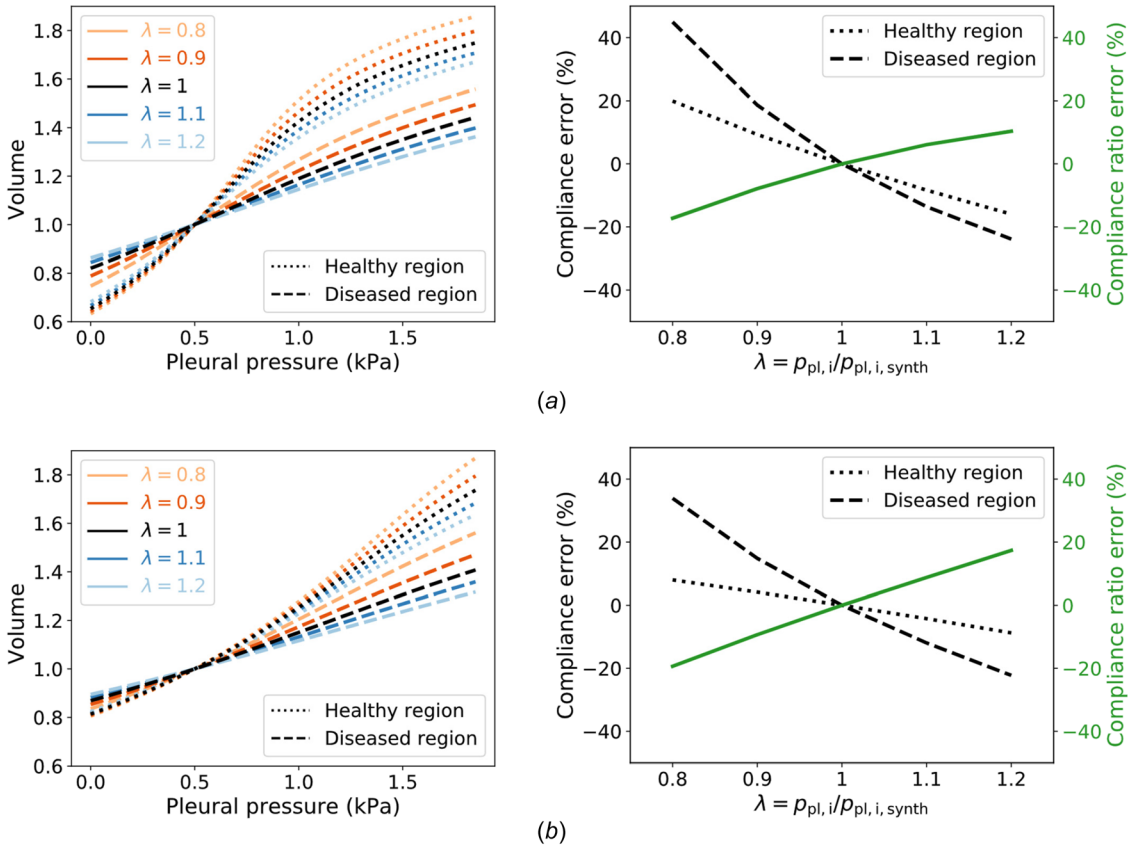

Fig. 4 Impact of the nonpatient-specific pressure applied in the model on the estimated compliance and compliance ratio (diseased compliance over healthy compliance), using both effective parameters (*a*) and rescaled parameters (*b*). λ is the ratio between the pressure used in the estimation and the pressure used to generate the synthetic data. For both types of parameters: (left) Visualization of pressure–volume curves for each pressure case (colored lines), compared to the pressure–volume curves obtained with the pressure used to create the synthetic data (black line); (right) Compliance error for each region as a function of the value of the pressure applied in the model, as well as the compliance ratio (C_h/C_d) error: (*a*) with effective parameters and (*b*) with rescaled parameters. (Color version online.)

Table 4 Evaluation of the use of rescaled parameters compared to effective parameters

	f_{disp}	f_{imag}
C1	–0.46%	–2.30%
P1	–2.77%	–0.46%
P2	+ 9.45%	+ 6.24%
P3	+13.09%	+9.32%

The values, expressed in %, are computed as $(f(\widetilde{\Theta}_{estim}) - f(\overline{\Theta}_{estim}))/f(\overline{\Theta}_{estim})$. They are presented for both criteria, f_{disp} and f_{imag}.

segmentations and compare the associated estimations to the estimation based on the physiological disease segmentation. We perform this study based on the data from subject P1 only. Twenty-six different lung divisions are defined. In all cases, the organ is divided into two parts by a plane defined by its normal and its position along the normal. We consider 13 normals corresponding to the edges and diagonals of a cube to define each plane. For each normal, we consider two divisions, by putting the diseased region on one side or the other, while maintaining the exact disease volume ratio, which is 31% for subject P1. For each division, the estimation of the material parameters is performed using the displacement-based criterion f_{disp} and the rescaled parameters only.

The results are presented in Fig. 6, as a box plot showing the distribution of the optimized values of the cost function. The two-region model is better in all the cases than the one-region model. This is expected, since the number of optimization parameters is higher. Out of 26 models based on arbitrary disease segmentations, 22 (i.e., 85%) lead to a larger optimal cost function,

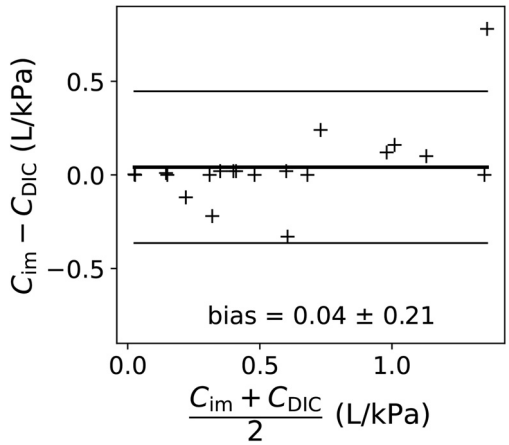

Fig. 5 Bland–Altman plot to compare the image and displacement criteria. The quantities used for the comparison are the compliances computed by both criteria. C_{DIC} and C_{im} are the compliances estimated with the displacement criterion and the image criterion, respectively.

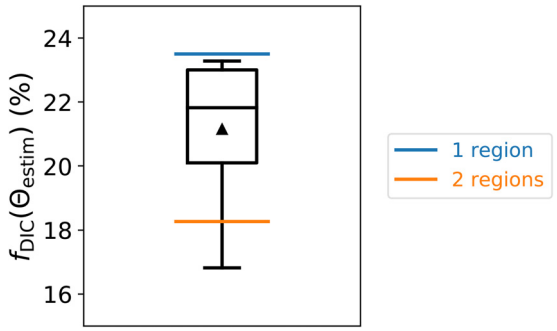

Fig. 6 Box plot representing the value of $f_{disp}(\widetilde{\Theta}_{estim})$ for the 26 cases of divisions into two regions. The box extends from the lower to upper quartile values. The horizontal black line is the median, whereas the triangle is the mean. The lower and upper whiskers extend to $Q_1-1.5(Q_3-Q_1)$ and $Q_3+1.5(Q_3-Q_1)$, respectively, with Q_1 and Q_3 the lower and upper quartiles, respectively. The box plot can be compared to the value of $f_{disp}(\Theta_{estim})$ in the case of the use of one region (blue line) and the case where the two regions come from the disease segmentation (orange line). (Color version online.)

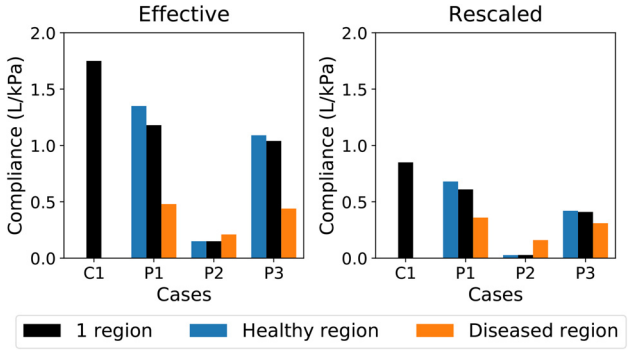

Fig. 7 Effective and rescaled compliances estimated for each subject. For each case, the global compliance, in black, is estimated with a one-region model, whereas the compliance of both healthy and diseased regions, in blue and orange, respectively, are estimated with a two-region model. For the control case C1, only the global compliance is estimated. Two types of compliance are estimated: (left) the effective compliance, and (right) the rescaled compliance. (Color version online.)

i.e., a worst model-data fit, compared to the model based on physiological disease segmentation.

In order to further analyze these statistical results, a Shapiro-Wilk test is first performed to determine whether the distribution is normally distributed. The p-value is 0.13%, which is not enough to accept the hypothesis of a normal distribution. Thus, a nonparametric Mann–Whitney U test is performed to evaluate if the optimized cost function of the two-region model based on the disease segmentation is smaller than the optimized cost function of a two-region model based on random segmentation. The resulting p-value is 13.7%, which is rather small, but not small enough to conclude with certainty. However, to put this value into perspective, we also tested that the optimized cost function of a random two-region model is smaller than the optimized cost functions of a one-region model, which is indeed certain since the parameter space of the one-region model is contained into the parameter space of the two-region model, and found a p-value of 5.4%. This suggests that more data is required to conclude with certainty. Nevertheless, we conclude from this analysis that the two-region model based on physiological disease segmentation almost certainly better fits the data than a two-region model with arbitrary disease segmentation.

3.3 Clinically Relevant Analysis. The results in this Section are obtained with the image criterion f_{imag}, since we justified previously that both criteria give statistically equivalent results.

3.3.1 Regional Compliances. The global pulmonary compliance is a common biomarker for clinicians to study the impact of pulmonary fibrosis on the lungs. With our model, the regional compliance can be also estimated, which gives information not accessible with direct measurements. The compliances, global and regional, are shown for each subject in Fig. 7. Note that compliances cannot be directly compared between subjects since the value is relative to the pleural pressure value used in this work, which is not patient-specific.

The results of the subject P2 are different from those of subjects P1 and P3. A very likely explanation for this lies in the very different amount of breathing, since the volume variation between end-exhalation and end-inhalation is only 14%, whereas it is between 80 and 90% for the other subjects. In what follows, we thus consider only subjects C1, P1, and P3.

For both patients P1 and P3, the global compliance is between healthy and diseased compliances, which can be easily understood since the global compliance aggregates the contributions of both regions. Moreover, the healthy region is more compliant than the diseased region, which is consistent with the current knowledge of pulmonary fibrosis [6,58].

For subjects C1, P1, and P3, effective compliance is smaller than rescaled compliance, which is expected since it is directly impacted by the porosity. More importantly, for patients P1 and P3, the ratio between healthy and diseased compliances is larger for effective parameters compared to rescaled parameters. This is also a consequence of the fact that rescaled parameters are less dependent on the porosity.

3.3.2 Stress Distribution. It is assumed that mechanics plays a major role in the pulmonary fibrosis evolution. Indeed, the assumption of a mechanical vicious circle in place for this disease has been formulated: fibrosis leads to stiffer tissue and increased stresses, which activates the production of collagen fibers by fibroblasts and induces still more fibrosis [5,8,59,60]. Our model allows to investigate the impact of the disease on the stress field, as shown for patient P1 in Fig. 8. It can be observed that the stress field is largely heterogeneous close to the interface between the two regions, i.e., the healthy and the diseased regions. In some interfacial areas, the stress is up to twice as large as further away from the interface. This stress concentration seems to support the mechanical vicious circle assumption, although a more quantitative analysis, with more data, would be necessary to conclude with certainty.

4 Discussion

In this paper, we introduced a personalization procedure for a recent pulmonary poromechanical model, which relies exclusively on routine clinical data, namely, thoracic 3D CT images. In particular, during the model personalization, patient-specific regional mechanical parameters are estimated, which cannot be measured noninvasively in vivo. To demonstrate its applicability and investigate its performance, the model personalization has been applied to one control and three diseased patients datasets. We now discuss several aspects of the personalization procedure, including current limitations and potential improvements.

4.1 Quasi-Static Assumption. Since only two images are acquired in routine clinical practice, we used a quasi-static lung model, assuming the two images correspond to static equilibrium. This could be revisited with the advancement of dynamic thoracic magnetic resonance [61] or CT imaging. Our model would then need to be updated to account for inertia and viscosity [62,63]. Furthermore, going from static to dynamic imaging would remove

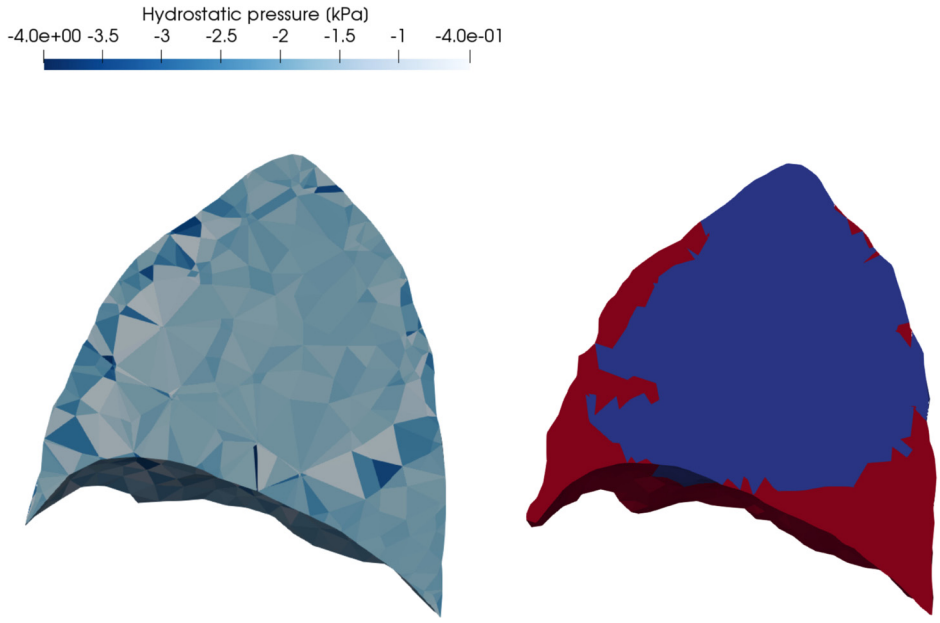

Fig. 8 Comparison of the mixture hydrostatic pressure (i.e., trace of Cauchy stress tensor) and the disease segmentation in the same slice. (left) Visualization of the mixture hydrostatic pressure in a sagittal slice of the lung. (right) Visualization of the segmentation of the fibrosis. The fibrotic region is in red, whereas the healthy region is in blue. (Color version online.)

any potential stress relaxation effect associated with breath-holding.

4.2 Two-Phase Mixture Assumption. The model currently only considers a two-phase mixture (solid + air), and does not represent explicitly structural components such as fissures, airway structures, etc. They are, however, implicitly taken into account through the heterogeneous porosity field extracted from the images and projected onto the mesh, although the underlying assumption is that the stiffness of the solid part of the mixture is homogeneous within one region of the mesh. Nevertheless, the impact of adding an explicit representation of the fissures or the airway tree [64], with a specific constitutive law, on the model personalization should be investigated.

4.3 Pleural Pressure. As discussed in Sec. 3.1.2, the results presented in this paper are relative to the pleural pressure applied at end-exhalation and end-inhalation, since no patient-specific pressure is available. Consequently, the estimated compliances are relative to that pressure. Measuring the patient-specific pressure would allow to compute the absolute compliance and to make comparisons between subjects. Such data could be acquired using an esophageal balloon to measure the esophageal pressure, considered as very close to the pleural pressure [65–67], under the scanner. However, this measurement is not part of the clinical routine for patients suffering from pulmonary fibrosis. Alternatively, in future studies we could prescribe the compliance in the healthy region and estimate the pleural pressure together with the compliance of the fibrotic region.

4.4 Effective Versus Rescaled Potentials. The choice of using poromechanics was made notably to take into account the porosity of the lungs. However, as seen in Sec. 3.1.3, the use of effective potentials, which do not explicitly take into account porosity variations and are thus equivalent to a simple hyperelastic model, still displays a good performance. Moreover, as seen in Sec. 3.2.1, if for subjects C1 and P1 the model based on rescaled potentials better fits the data than the model based on effective potentials, it is not the case for subjects P2 and P3. One possible explanation is that for subjects C1 and P1, the porosity variations are rather smooth and induce strain variations that can be well represented by the finite element mesh, in the tracking and in the model; in this case, taking into account the local variations of porosity allows the model to better fit the data. Conversely, for subjects P2 and P3, the fibrotic regions are more patchy, such that the porosity variations, and thus the strain variations, are sharper and cannot be well represented over the finite element mesh; in this case the cost function is biased, which affects the estimation. A thorough analysis of the impact of mesh size, for both the tracking and the model itself, will be conducted in a subsequent study.

Nevertheless, even with the current modeling and personalization approach, the use of poromechanics has several advantages compared to standard hyperelasticity. First, as illustrated in Refs. [23] and [24], it allows to study various breathing regimes, including ventilated breathing. Moreover, it brings useful information about the material properties and stress state of the solid constituent, which cannot be measured in vivo. Furthermore, it allows to introduce the effect of porosity onto the mixture behavior, which we did here in the simplest possible way with the rescaled parameters. Such a model could also be used to study the impact of porosity or of porosity gradient in the lungs.

4.5 Displacement Versus Image Criteria. Two criteria have been investigated: one using a displacement field, like in FEMU approaches, and one using images directly, as an integrated image correlation approach. The displacement criterion is easier to understand since the result can be expressed in terms of a length, the RMSE error. For example, the RMSE errors for the cases P1 and P3 are 4.9 mm and 11.4 mm, respectively. It allows to quantify the accuracy of the method in a meaningful way, especially for clinicians. However, the use of the displacement method requires to perform image registration between both images, which introduces another source of error. On the other hand, the image criterion includes the same term of similarity between images than in image registration and allows to perform in one step what is done in two steps with the displacement criterion. Nevertheless, the optimized value of this criterion is less meaningful. Moreover, because of the current choice for the shape

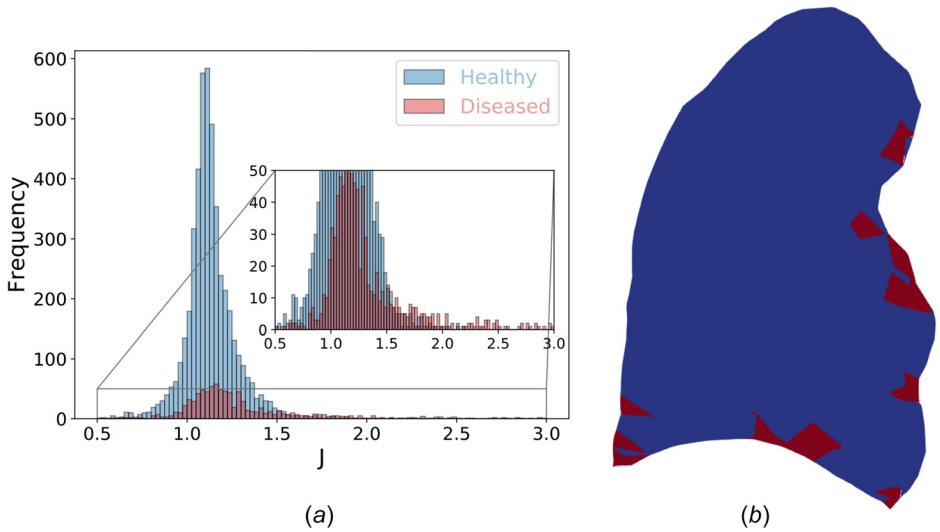

Fig. 9 Details about the patient P2 to understand the related results. (*a*) Distribution of the local variation of volume J for each region. In the healthy region, $J_{healthy} = 1.13 \pm 0.15$, whereas in the diseased region, $J_{diseased} = 1.32 \pm 0.42$. (*b*) Visualization of the regions in a plane: the blue part is the healthy region, whereas the red part is the diseased region. (Color version online.)

registration term, this criterion is not differentiable, which restricts its use in other minimization tools.

4.6 Disease Segmentation. An important clinical outcome of our proposed modeling and personalization pipeline is the estimation of regional compliances, in the healthy and diseased regions of the lungs. We have shown that a two-region model is more accurate with respect to the data than a one-region model, since more optimization degrees-of-freedom are present in a two-region model. Based on our study, in most cases the definition of two regions matching with the disease segmentation also brings better results than the definition of two random regions, which is a promising result. However, more data is needed to further substantiate this finding.

4.7 Regional Homogeneity. We assumed homogeneous material properties in each region. Note however that, as already mentioned in Sec. 2.2.2, in the case of rescaled potentials the actual behavior is heterogeneous due to the porosity field extracted from the images. Nevertheless, this assumption could be further studied by defining several regions for the control subject or by defining several healthy and diseased regions for the patients. Then, the variability of estimated material parameters in each region would give information about the lung inhomogeneity.

4.8 Parameter Optimization. If inverse problems are generally ill-posed, the one formulated in the proposed personalization procedure has relatively few parameters (one for controls, two for patients) and relatively large data (the full displacement field or image) so that parameter convergence was always smooth and fast. Nevertheless, a fully quantitative analysis of parameter identifiability would help to gain confidence in the personalization procedure.

4.9 Clinical Implications. The results obtained in this work are consistent with the current knowledge of the disease. Indeed, the effective global compliance of the control subject C1 is 1.75 L/kPa, whereas Ref. [68] showed that the global compliance of one lung is 1.67 ± 0.55 L/kPa. The result has an adequate value, even though it is relative to the nonpatient-specific pressure of the model. Then, the personalization for the diseased subjects led to a stiffer diseased region than the healthy region, which is consistent with the literature [5,69–71]. More precisely, when considering rescaled parameters, we obtained that the solid tissue in the diseased region is stiffer than in the healthy region, which is an information difficult to measure experimentally. The personalization pipeline allows then to quantify the stiffening of the organ with the pulmonary fibrosis.

When applied with more patients, stiffening quantification obtained from the personalized model can be studied in relation to other clinical quantities in order to investigate any correlation. In particular, stiffening could be linked to the disease severity, either determined by the volume of the diseased region or diffusing capacity of the lung for carbon monoxide, or the disease decline at 6- or 12-months.

The finding of a stress concentration at the border of the fibrotic region is also a result of major clinical interest. It is a first step toward the confirmation of the hypothesis of the mechanical vicious circle which would govern pulmonary fibrosis. The validation of this phenomenon on more cases would help to better understand and then predict the disease progress.

Some limitations appeared with the patient P2. The diseased region for this patient appeared to have a similar or higher compliance than that of the healthy region, which seems inconsistent with what is known on pulmonary fibrosis. One hypothesis would be that it corresponds to some specific characteristics of the disease. After further investigations, it is more likely that the cause comes from the data itself. Indeed, the image registration does not show smaller deformation in the diseased region. The diseased region is also quite small (about 7% of the total volume), very discontinuous, and not significantly thick compared to the element size, as can be seen in Fig. 9. A finer mesh might be required to analyze patients with such disease patterns.

4.10 Experimental Validation. In order to fully validate the compliances estimated from the images using our personalized modeling procedure, more controlled experiments should be used. Ex vivo experimental procedures including rich instrumentations have recently been developed for lung tissue [33,72]. They could be used in conjunction with in vivo imaging.

5 Conclusion

We presented a poromechanical model of the lung, which is personalized to patients using routine clinical images. Applied on one control and three diseased subjects suffering from idiopathic

pulmonary fibrosis, it allows in particular to quantify the regional pulmonary compliance. The results are consistent with the knowledge of the disease, especially as regards the stiffening of the fibrotic regions. The estimation process brings information about regional compliances, which are not available in vivo. This work brings a proof of concept and still needs to be applied with more patients before being used in clinical routine for diagnosis purposes. A first step toward a better understanding of the IPF physiology is also provided by the evidence of a stress concentration at the border of the fibrotic zone, which would confirm the hypothesis of the mechanical vicious circle underlying IPF progress. In the longer term, this personalized model could be used with longitudinal data to study the prognosis of the disease, as well as the mechanical impact of drugs.

Funding Data

- French National Research Agency (ANR-19-CE45-0007; Funder ID: 10.13039/501100001665).

References

[1] Walsh, S. L., Maher, T. M., Kolb, M., Poletti, V., Nusser, R., Richeldi, L., Vancheri, C., Wilsher, M. L., Antoniou, K. M., Behr, J., Bendstrup, E., Brown, K., Calandriello, L., Corte, T. J., Cottin, V., Crestani, B., Flaherty, K., Glaspole, I., Grutters, J., Inoue, Y., Kokosi, M., Kondoh, Y., Kouranos, V., Kreuter, M., Johannson, K., Judge, E., Ley, B., Margaritopoulos, G., Martinez, F. J., Molina-Molina, M., Morais, A., Nunes, H., Raghu, G., Ryerson, C. J., Selman, M., Spagnolo, P., Taniguchi, H., Tomassetti, S., Valeyre, D., Wijsenbeek, M., Wuyts, W., Hansell, D., and Wells, A., 2017, "Diagnostic Accuracy of a Clinical Diagnosis of Idiopathic Pulmonary Fibrosis: An International Case-Cohort Study," Eur. Respir. J., **50**(2), p. 1700936.

[2] Fernández Pérez, E. R., Daniels, C. E., Schroeder, D. R., St Sauver, J., Hartman, T. E., Bartholmai, B. J., Yi, E. S., and Ryu, J. H., 2010, "Incidence, Prevalence, and Clinical Course of Idiopathic Pulmonary Fibrosis: A Population-Based Study," Chest, **137**(1), pp. 129–137.

[3] Walsh, S. L. F., Wells, A. U., Desai, S. R., Poletti, V., Piciucchi, S., Dubini, A., Nunes, H., Valeyre, D., Brillet, P.-Y., Kambouchner, M., Morais, A., Pereira, J. M., Moura, C. S., Grutters, J. C., van den Heuvel, D. A., van Es, H. W., van Oosterhout, M. F., Seldenrijk, C. A., Bendstrup, E., Rasmussen, F., Madsen, L. B., Gooptu, B., Pomplun, S., Taniguchi, H., Fukuoka, J., Johkoh, T., Nicholson, A. G., Sayer, C., Edmunds, L., Jacob, J., Kokosi, M. A., Myers, J. L., Flaherty, K. R., and Hansell, D. M., 2016, "Multicentre Evaluation of Multidisciplinary Team Meeting Agreement on Diagnosis in Diffuse Parenchymal Lung Disease: A Case-Cohort Study," Lancet Respir. Med., **4**(7), pp. 557–565.

[4] Flaherty, K. R., Fell, C. D., Huggins, J. T., Nunes, H., Sussman, R., Valenzuela, C., Petzinger, U., Stauffer, J. L., Gilberg, F., Bengus, M., and Wijsenbeek, M., 2018, "Safety of Nintedanib Added to Pirfenidone Treatment for Idiopathic Pulmonary Fibrosis," Eur. Respir. J., **52**(2), p. 1800230.

[5] Haak, A. J., Tan, Q., and Tschumperlin, D. J., 2018, "Matrix Biomechanics and Dynamics in Pulmonary Fibrosis," Matrix Biol., **73**, pp. 64–76.

[6] Plantier, L., Cazes, A., Dinh-Xuan, A.-T., Bancal, C., Marchand-Adam, S., and Crestani, B., 2018, "Physiology of the Lung in Idiopathic Pulmonary Fibrosis," Eur. Respir. Rev., **27**(147), p. 170062.

[7] Carloni, A., Poletti, V., Fermo, L., Bellomo, N., and Chilosi, M., 2013, "Heterogeneous Distribution of Mechanical Stress in Human Lung: A Mathematical Approach to Evaluate Abnormal Remodeling in IPF," J. Theor. Biol., **332**, pp. 136–140.

[8] Hinz, B., and Suki, B., 2016, "Does Breathing Amplify Fibrosis?," Am. J. Respir. Crit. Care Med., **194**(1), pp. 9–11.

[9] Chabiniok, R., Moireau, P., Lesault, P.-F., Rahmouni, A., Deux, J.-F., and Chapelle, D., 2012, "Estimation of Tissue Contractility From Cardiac Cine-MRI Using a Biomechanical Heart Model," Biomech. Model. Mechanobiol., **11**(5), pp. 609–630.

[10] Genet, M., Chuan Lee, L., Ge, L., Acevedo-Bolton, G., Jeung, N., Martin, A., Cambronero, N., Boyle, A., Yeghiazarians, Y., Kozerke, S., and Guccione, J. M., 2015, "A Novel Method for Quantifying Smooth Regional Variations in Myocardial Contractility Within an Infarcted Human Left Ventricle Based on Delay-Enhanced Magnetic Resonance Imaging," ASME J. Biomech. Eng., **137**(8), p. 081009.

[11] Chabiniok, R., Wang, V. Y., Hadjicharalambous, M., Asner, L., Lee, J., Sermesant, M., Kuhl, E., Young, A. A., Moireau, P., Nash, M. P., Chapelle, D., and Nordsletten, D. A., 2016, "Multiphysics and Multiscale Modelling, Data–Model Fusion and Integration of Organ Physiology in the Clinic: Ventricular Cardiac Mechanics," Interface Focus, **6**(2), p. 20150083.

[12] Lee, L. C., Genet, M., Dang, A. B., Ge, L., Guccione, J. M., and Ratcliffe, M. B., 2014, "Applications of Computational Modeling in Cardiac Surgery," J. Card. Surg., **29**(3), pp. 293–302.

[13] Krishnamurthy, A., Villongco, C. T., Chuang, J., Frank, L. R., Nigam, V., Belezzuoli, E., Stark, P., Krummen, D. E., Narayan, S. M., Omens, J. H., McCulloch, A. D., and Kerckhoffs, R. C. P., 2013, "Patient-Specific Models of Cardiac Biomechanics," J. Comput. Phys., **244**, pp. 4–21.

[14] Smith, N. P., de Vecchi, A., McCormick, M., Nordsletten, D. A., Camara, O., Frangi, A. F., Delingette, H., Sermesant, M., Relan, J., Ayache, N., Krueger, M. W., Schulze, W. H. W., Hose, R., Valverde, I., Beerbaum, P., Staicu, C., Siebes, M., Spaan, J., Hunter, P. J., Weese, J., Lehmann, H., Chapelle, D., and Rezavi, R., 2011, "euHeart: Personalized and Integrated Cardiac Care Using Patient-Specific Cardiovascular Modelling," Interface Focus, **1**(3), pp. 349–64.

[15] Álvarez-Barrientos, F., Hurtado, D. E., and Genet, M., 2021, "Pressure-Driven Micro-Poro-Mechanics: A Variational Framework for Modeling the Response of Porous Materials," Int. J. Eng. Sci., **169**, p. 103586.

[16] Concha, F., Sarabia-Vallejos, M., and Hurtado, D. E., 2018, "Micromechanical Model of Lung Parenchyma Hyperelasticity," J. Mech. Phys. Solids, **112**, pp. 126–144.

[17] Birzle, A. M., Hobrack, S. M. K., Martin, C., Uhlig, S., and Wall, W. A., 2019, "Constituent-Specific Material Behavior of Soft Biological Tissue: Experimental Quantification and Numerical Identification for Lung Parenchyma," Biomech. Model. Mechanobiol., **18**(5), pp. 1383–1400.

[18] Roth, C. J., Ismail, M., Yoshihara, L., and Wall, W. A., 2017, "A Comprehensive Computational Human Lung Model Incorporating Inter-Acinar Dependencies: Application to Spontaneous Breathing and Mechanical Ventilation," Int. J. Numer. Methods Biomed. Eng., **33**(1), p. e02787.

[19] Yin, Y., Choi, J., Hoffman, E. A., Tawhai, M. H., and Lin, C.-L., 2010, "Simulation of Pulmonary Air Flow With a Subject-Specific Boundary Condition," J. Biomech., **43**(11), pp. 2159–2163.

[20] Berger, L., Bordas, R., Burrowes, K., Grau, V., Tavener, S., and Kay, D., 2016, "A Poroelastic Model Coupled to a Fluid Network With Applications in Lung Modelling: A Poroelastic Model Coupled to a Fluid Network With Applications in Lung Modelling," Int. J. Numer. Methods Biomed. Eng., **32**(1), p. e02731.

[21] Tawhai, M. H., Nash, M. P., Lin, C.-L., and Hoffman, E. A., 2009, "Supine and Prone Differences in Regional Lung Density and Pleural Pressure Gradients in the Human Lung With Constant Shape," J. Appl. Physiol., **107**(3), pp. 912–920.

[22] Burrowes, K., Swan, A., Warren, N., and Tawhai, M., 2008, "Towards a Virtual Lung: Multi-Scale, Multi-Physics Modelling of the Pulmonary System," Philos. Trans. R. Soc. A Math., Phys. Eng. Sci., **366**(1879), pp. 3247–3263(2008).

[23] Patte, C., 2020, "Personalized Pulmonary Mechanics: Modeling, Estimation and Application to Pulmonary Fibrosis," Ph.D. thesis, Inria, École Polytechnique, France.

[24] Patte, C., Genet, M., and Chapelle, D., 2022, "A Quasi-Static Poromechanical Model of the Lungs," Biomech. Model. Mechanobiol., **21**(2), pp. 527–551.

[25] Patte, C., Genet, M., Fetita, C., Brillet, P.-Y., and Chapelle, D., 2019, "Mécanique Pulmonaire Personnalisée: Modélisation et estimation - Application à la Fibrose Pulmonaire," 14ème Colloque National en Calcul Des Structures (CSMA2019), Presqu'île de Giens, Var, France, May 13–17.

[26] Chapelle, D., and Moireau, P., 2014, "General Coupling of Porous Flows and Hyperelastic Formulations—From Thermodynamics Principles to Energy Balance and Compatible Time Schemes," Eur. J. Mech. B/Fluids, **46**, pp. 82–96.

[27] Biot, M. A., and Temple, G., 1972, "Theory of Finite Deformations of Porous Solids," Indiana Univ. Math. J., **21**(7), pp. 597–620.

[28] Coussy, O., 2004, *Poromechanics*, Wiley, Chichester, UK.

[29] Fetita, C., Tarando, S., Brillet, P.-Y., and Grenier, P. A., 2016, "Robust Lung Identification in MSCT Via Controlled Flooding and Shape Constraints: Dealing With Anatomical and Pathological Specificity," SPIE Paper No. 97881A.

[30] Boucneau, T., 2019, "Magnetic Resonance Imaging of Respiratory Mechanics," Ph.D. thesis, Université Paris-Saclay, France.

[31] Gargani, L., 2011, "Lung Ultrasound: A New Tool for the Cardiologist," Cardiovasc. Ultrasound, **9**(1), p. 6.

[32] Cottin, V., Crestani, B., Valeyre, D., Wallaert, B., Cadranel, J., Dalphin, J., Delaval, P., Israel-Biet, D., Kessler, R., Reynaud-Gaubert, M., Cordier, J., Aguilaniu, B., Bouquillon, B., Carré, P., Danel, C., Faivre, J.-B., Ferreti, G., Just, N., Kouzan, S., Lebargy, F., Marchand Adam, S., Philippe, B., Prévot, G., Stach, B., and Thivolet-Béjui, F., 2013, "Recommandations Pratiques Pour le Diagnostic et la Prise en Charge de la Fibrose Pulmonaire Idiopathique. Élaborées Par le Centre National de Référence et Les Centres de Compétence Pour Les Maladies Pulmonaires Rares Sous L'égide de la Société de Pneumologie de Langue Française," Rev. Mal. Respir., **30**(10), pp. 879–902.

[33] Mariano, C. A., Sattari, S., Maghsoudi-Ganjeh, M., Tartibi, M., Lo, D. D., and Eskandari, M., 2020, "Novel Mechanical Strain Characterization of Ventilated Ex Vivo Porcine and Murine Lung Using Digital Image Correlation," Front. Physiol., **11**(600492).

[34] Govindjee, S., and Mihalic, P. A., 1998, "Computational Methods for Inverse Deformations in Quasi-Incompressible Finite Elasticity," Int. J. Numer. Methods Eng., **43**(5), pp. 821–838.

[35] Alnæs, M., Blechta, J., Hake, J., Johansson, A., Kehlet, B., Logg, A., Richardson, C., Ring, J., Rognes, M. E., and Wells, G. N., 2015, "The FEniCS Project Version 1.5," Arch. Numer. Softw., **3**(100).

[36] Logg, A., Mardal, K., and Wells, G., 2012, *Automated Solution of Differential Equations by the Finite Element Method: The FEniCS Book* (Lecture Notes in Computational Science and Engineering), Springer, Berlin Heidelberg.

[37] Ritter, F., Boskamp, T., Homeyer, A., Laue, H., Schwier, M., Link, F., and Peitgen, H., 2011, "Medical Image Analysis," IEEE Pulse, **2**(6), pp. 60–70.

[38] Geuzaine, C., and Remacle, J.-F., 2009, "Gmsh: A Three-Dimensional Finite Element Mesh Generator With Built-In Pre- and Post-Processing Facilities," Int. J. Numer. Methods Eng., **79**(11), pp. 1309–1331.

[39] Remacle, J.-F., Geuzaine, C., Compere, G., and Marchandise, E., 2010, "High Quality Surface Remeshing Using Harmonic Maps," Int. J. Numer. Methods Eng., **83**(4), pp. 403–425.
[40] Genet, M., Stoeck, C., von Deuster, C., Lee, L., and Kozerke, S., 2018, "Equilibrated Warping: Finite Element Image Registration With Finite Strain Equilibrium Gap Regularization," Med. Image Anal., **50**, pp. 1–22.
[41] Hedlund, L., Vock, P., and Effmann, E., 1983, "Evaluating Lung Density by Computed Tomography," Semin. Respir. Crit. Care Med., **5**(01), pp. 76–88.
[42] Yushkevich, P. A., Piven, J., Hazlett, H. C., Smith, R. G., Ho, S., Gee, J. C., and Gerig, G., 2006, "User-Guided 3D Active Contour Segmentation of Anatomical Structures: Significantly Improved Efficiency and Reliability," NeuroImage, **31**(3), pp. 1116–1128.
[43] Genet, M., Stoeck, C., von Deuster, C., Lee, L. C., Guccione, J. M., and Kozerke, S., 2016, "Finite Element Digital Image Correlation for Cardiac Strain Analysis From 3D Whole-Heart Tagging," ISMRM 24rd Annual Meeting and Exhibition 2016, Singapore, May 7–13.
[44] Hurtado, D. E., Villarroel, N., Retamal, J., Bugedo, G., and Bruhn, A., 2016, "Improving the Accuracy of Registration-Based Biomechanical Analysis: A Finite Element Approach to Lung Regional Strain Quantification," IEEE Trans. Med. Imaging, **35**(2), pp. 580–588.
[45] Vishnevskiy, V., Gass, T., Szekely, G., Tanner, C., and Goksel, O., 2017, "Isotropic Total Variation Regularization of Displacements in Parametric Image Registration," IEEE Trans. Med. Imaging, **36**(2), pp. 385–395.
[46] Yin, Y., Hoffman, E. A., and Lin, C.-L., 2009, "Mass Preserving Nonrigid Registration of CT Lung Images Using Cubic B-Spline: Mass Preserving Nonrigid Registration of CT Lung Images," Med. Phys., **36**(9Part1), pp. 4213–4222.
[47] Gullberg, G. T., 2005, "Measurement of Strain in the Left Ventricle During Diastole With cine-MRI and Deformable Image Registration," ASME J. Biomech. Eng., **127**(7), p. 1195.
[48] Claire, D., Hild, F., and Roux, S., 2004, "A Finite Element Formulation to Identify Damage Fields: The Equilibrium Gap Method," Int. J. Numer. Methods Eng., **61**(2), pp. 189–208.
[49] Avril, S., Bonnet, M., Bretelle, A.-S., Grédiac, M., Hild, F., Ienny, P., Latourte, F., Lemosse, D., Pagano, S., Pagnacco, E., and Pierron, F., 2008, "Overview of Identification Methods of Mechanical Parameters Based on Full-Field Measurements," Exp. Mech., **48**(4), pp. 381–402.
[50] Azzouna, M. B., Feissel, P., and Villon, P., 2013, "Identification of Elastic Properties From Full-Field Measurements: A Numerical Study of the Effect of Filtering on the Identification Results," Meas. Sci. Technol., **24**(5), p. 055603.
[51] Hild, F., and Roux, S., 2006, "Digital Image Correlation: From Displacement Measurement to Identification of Elastic Properties - A Review," Strain, **42**(2), pp. 69–80.
[52] Leclerc, H., Périé, J.-N., Roux, S., and Hild, F., 2009, "Integrated Digital Image Correlation for the Identification of Mechanical Properties," *Computer Vision/Computer Graphics CollaborationTechniques*, Gagalowicz, A. and Philips, W., eds., Vol. 5496, Springer Berlin Heidelberg, Berlin, Heidelberg, pp. 161–171.
[53] Réthoré, J., Roux, S., and Hild, F., 2009, "An Extended and Integrated Digital Image Correlation Technique Applied to the Analysis of Fractured Samples: The Equilibrium Gap Method as a Mechanical Filter," Eur. J. Comput. Mech., **18**(3–4), pp. 285–306.
[54] Taha, A. A., and Hanbury, A., 2015, "Metrics for Evaluating 3D Medical Image Segmentation: Analysis, Selection, and Tool," BMC Med. Imaging, **15**(1), p. 29.
[55] Hansen, N., 2016, "The CMA Evolution Strategy: A Tutorial," Cornell University, Ithaca, NY.
[56] Hansen, N., and Auger, A., 2014, "Principled Design of Continuous Stochastic Search: From Theory to Practice," *Theory and Principled Methods for the Design of Metaheuristics*, Borenstein, Y. and Moraglio, A., eds., Springer Berlin Heidelberg, Berlin, Heidelberg, pp. 145–180.
[57] Škardová, K., Rambausek, M., Chabiniok, R., and Genet, M., 2019, "Mechanical and Imaging Models-Based Image Registration," VipIMAGE (Lecture Notes in Computational Vision and Biomechanics), Tavares, J. M. R. S. and Natal Jorge, R. M., eds., Springer International Publishing, Cham, Switzerland, pp. 77–85.
[58] Gibson, G., 2001, "Lung Volumes and Elasticity," Clin. Chest Med., **22**(4), pp. 623–635.
[59] Liu, F., Mih, J. D., Shea, B. S., Kho, A. T., Sharif, A. S., Tager, A. M., and Tschumperlin, D. J., 2010, "Feedback Amplification of Fibrosis Through Matrix Stiffening and COX-2 Suppression," J. Cell Biol., **190**(4), pp. 693–706.
[60] Wu, H., Yu, Y., Huang, H., Hu, Y., Fu, S., Wang, Z., Shi, M., Zhao, X., Yuan, J., Li, J., Yang, X., Bin, E., Wei, D., Zhang, H., Zhang, J., Yang, C., Cai, T., Dai, H., Chen, J., and Tang, N., 2020, "Progressive Pulmonary Fibrosis is Caused by Elevated Mechanical Tension on," Alveolar Stem Cells. Cell, **180**(1), pp. 107–121.
[61] Boucneau, T., Fernandez, B., Larson, P., Darrasse, L., and Maître, X., 2020, "3D Magnetic Resonance Spirometry," Sci. Rep., **10**(1), p. 9649.
[62] Birzle, A. M., and Wall, W. A., 2019, "A Viscoelastic Nonlinear Compressible Material Model of Lung Parenchyma – Experiments and Numerical Identification," J. Mech. Behav. Biomed. Mater., **94**, pp. 164–175.
[63] Sattari, S., Mariano, C. A., Vittalbabu, S., Velazquez, J. V., Postma, J., Horst, C., Teh, E., Nordgren, T. M., and Eskandari, M., 2020, "Introducing a Custom-Designed Volume-Pressure Machine for Novel Measurements of Whole Lung Organ Viscoelasticity and Direct Comparisons Between Positive- and Negative-Pressure Ventilation," Front. Bioengin. Biotechnol., **8**, p. 578762.
[64] Lo, P., van Ginneken, B., Reinhardt, J. M., Yavarna, T., de Jong, P. A., Irving, B., Fetita, C., Ortner, M., Pinho, R., Sijbers, J., Feuerstein, M., Fabijanska, A., Bauer, C., Beichel, R., Mendoza, C. S., Wiemker, R., Lee, J., Reeves, A. P., Born, S., Weinheimer, O., van Rikxoort, E. M., Tschirren, J., Mori, K., Odry, B., Naidich, D. P., Hartmann, I., Hoffman, E. A., Prokop, M., Pedersen, J. H., and de Bruijne, M., 2012, "Extraction of Airways From CT (EXACT'09)," IEEE Trans. Med. Imaging, **31**(11), pp. 2093–2107.
[65] Agostoni, E., 1972, "Mechanics of the Pleural Space," Physiol. Rev., **52**(1), pp. 57–128.
[66] Akoumianaki, E., Maggiore, S. M., Valenza, F., Bellani, G., Jubran, A., Loring, S. H., Pelosi, P., Talmor, D., Grasso, S., Chiumello, D., Guérin, C., Patroniti, N., Ranieri, V. M., Gattinoni, L., Nava, S., Terragni, P.-P., Pesenti, A., Tobin, M., Mancebo, J., and Brochard, L., 2014, "The Application of Esophageal Pressure Measurement in Patients With Respiratory Failure," Am. J. Respir. Crit. Care Med., **189**(5), pp. 520–531.
[67] Hoppin, F. G., Green, I. D., and Mead, J., 1969, "Distribution of Pleural Surface Pressure in Dogs," J. Appl. Physiol., **27**(6), pp. 863–873.
[68] Galetke, W., Feier, C., Muth, T., Ruehle, K.-H., Borsch-Galetke, E., and Randerath, W., 2007, "Reference Values for Dynamic and Static Pulmonary Compliance in Men," Respir. Med., **101**(8), pp. 1783–1789.
[69] Booth, A. J., Hadley, R., Cornett, A. M., Dreffs, A. A., Matthes, S. A., Tsui, J. L., Weiss, K., Horowitz, J. C., Fiore, V. F., Barker, T. H., Moore, B. B., Martinez, F. J., Niklason, L. E., and White, E. S., 2012, "Acellular Normal and Fibrotic Human Lung Matrices as a Culture System for In Vitro Investigation," Am. J. Respir. Crit. Care Med., **186**(9), pp. 866–876.
[70] Georges, P. C., Hui, J.-J., Gombos, Z., McCormick, M. E., Wang, A. Y., Uemura, M., Mick, R., Janmey, P. A., Furth, E. E., and Wells, R. G., 2007, "Increased Stiffness of the Rat Liver Precedes Matrix Deposition: Implications for Fibrosis," Am. J. Physiol. Gastrointest. Liver Physiol., **293**(6), pp. G1147–G1154.
[71] Liu, F., Lagares, D., Choi, K. M., Stopfer, L., Marinković, A., Vrbanac, V., Probst, C. K., Hiemer, S. E., Sisson, T. H., Horowitz, J. C., Rosas, I. O., Fredenburgh, L. E., Feghali-Bostwick, C., Varelas, X., Tager, A. M., and Tschumperlin, D. J., 2015, "Mechanosignaling Through Yap and TAZ Drives Fibroblast Activation and Fibrosis," Am. J. Physiol.-Lung Cell. Mol. Physiol., **308**(4), pp. L344–L357.
[72] Richardson, S., Gamage, T. P. B., HajiRassouliha, A., Jackson, T., Hedges, K., Clark, A., Taberner, A., Tawhai, M. H., and Nielsen, P. M. F., 2019, "Towards a Real-Time Full-Field Stereoscopic Imaging System for Tracking Lung Surface Deformation Under Pressure Controlled Ventilation," *Computational Biomechanics for Medicine*, Nielsen, P. M. F., Wittek, A., Miller, K., Doyle, B., Joldes, G. R., and Nash, M. P., eds., Springer International Publishing, Cham, Switzerland, pp. 119–130.